Lattice dynamics and the nature of structural transitions in organolead halide perovskites

Riccardo Comin,[1,*] Michael K. Crawford,[2,3] Ayman H. Said,[4] Norman Herron,[5] William E. Guise,[2] Xiaoping Wang,[6] Pamela S. Whitfield,[6] Ankit Jain,[1] Xiwen Gong,[1] Alan J. H. McGaughey,[7] and Edward H. Sargent[1,†]

[1]*Department of Electrical and Computer Engineering, University of Toronto, 10 Kings College Road, Toronto, Ontario M5S 3G4, Canada*
[2]*DuPont Central Research and Development, Wilmington, Delaware 19803, USA*
[3]*Department of Physics and Astronomy, University of Delaware, Newark, Delaware 19716, USA*
[4]*Advanced Photon Source, Argonne National Lab, Argonne, Illinois 60439, USA*
[5]*DuPont Electronics and Communication Technologies, Wilmington, Delaware 19803, USA*
[6]*Chemical and Engineering Materials Division, Oak Ridge National Laboratory, Oak Ridge, Tennessee 37831, USA*
[7]*Mechanical Engineering Department, Carnegie Mellon University, Pittsburgh, Pennsylvania 15213, USA*
(Received 10 March 2016; revised manuscript received 25 July 2016; published 9 September 2016)

Organolead halide perovskites are a family of hybrid organic-inorganic compounds whose remarkable optoelectronic properties have been under intensive scrutiny in recent years. Here we use inelastic x-ray scattering to study low-energy lattice excitations in single crystals of methylammonium lead iodide and bromide perovskites. Our findings confirm the displacive nature of the cubic-to-tetragonal phase transition, which is further shown, using neutron and x-ray diffraction, to be close to a tricritical point. Lastly, we detect quasistatic symmetry-breaking nanodomains persisting well into the high-temperature cubic phase, possibly stabilized by local defects. These findings reveal key structural properties of these materials, and also bear important implications for carrier dynamics across an extended temperature range relevant for photovoltaic applications.

Structural phase transitions and the cubic-to-tetragonal lowering of the lattice symmetry have long been studied in cubic halide and oxide perovskites [1–4]. The nature of the phase transition is generally understood to be of the displacive type, involving the softening of a zone-edge mode (such as in $CsPbCl_3$, $SrTiO_3$, and $KMnF_3$) or a zone-center mode (such as in $PbTiO_3$) and the consequent frozen-in distortion of the lattice in the low-symmetry phase. This mechanism is accompanied by a change in symmetry which in reciprocal space is signalled by the emergence of a superlattice Bragg reflection at the wave vector where the phonon softening occurs. In hybrid lead halide perovskites, a materials platform which has catalyzed considerable attention in the field of optoelectronics in recent years [5], the crystal structure plays a fundamental role, exerting a direct feedback on the electronic structure and the band gap [6–8]. The resulting band structure and associated optical response are in turn crucial for photovoltaic and light emission applications, where spectral tunability is key for device performance and versatility. The influence of structural changes on the performance of perovskite-based solar devices has been explored previously from both an experimental [9] and a theoretical [10] viewpoint, across an extended temperature range relevant to photovoltaic functionality. Phenomenologically, it has been observed that the cubic-to-tetragonal phase transition has little effect on device performance, a finding that was later elucidated using *ab initio* molecular dynamics simulations. This investigation revealed that on a sub-ps timescale the carriers still experience a slightly distorted (i.e., noncubic) local environment, not dissimilar to that of the room-temperature tetragonal phase, thus lifting any discontinuity in the band structure and corresponding electrodynamics. A question then arises as to whether the local deviations from the cubic structure in the high-temperature phase are purely dynamic, or whether there is a static component, quenched by the presence of symmetry-breaking localized defects.

In order to assess such a scenario, in the present study we investigate the lattice dynamics of methylammonium (MA = CH_3NH_3) lead iodide ($MAPbI_3$) and bromide ($MAPbBr_3$) along the high-symmetry direction of the cubic phase of these compounds. $MAPbI_3$ crystallizes at room temperature in the tetragonal structure (space group $I4/mcm$) whereas $MAPbBr_3$ is found in the cubic phase (space group $Pm\bar{3}m$) and both compounds undergo a cubic-to-tetragonal first-order structural transition at $T_c = 327.5$ and 236.9 K, respectively [11]. With the intent of clarifying the mechanistic details of the cubic-to-tetragonal phase transition, we use x-ray powder diffraction and neutron scattering to analyze the changes in lattice symmetry via the superlattice Bragg reflection, which serves as the order parameter for the tetragonal structure. Additionally, we perform high-resolution inelastic x-ray scattering (IXS) measurements using the HERIX spectrometer at sector 30 at the Advanced Photon Source [12,13], in order to measure the dynamical structure factor in an extended portion of reciprocal space, and in the meV energy range. For these measurements, we synthesized crystals of $MAPbI_3$ and $MAPbBr_3$ using the inverse temperature crystallization method described in Refs. [14,15]. X-ray and neutron experiments have been performed at the superlattice reflection $(3/2,1/2,1/2)$, defined with respect to the cubic unit cell. In order to map out the complete phonon dispersion with IXS, we focused on reciprocal space directions connecting the Brillouin zone center point Γ [with wave vector $\mathbf{Q}_\Gamma = (H,K,L)$] to the zone edge high-symmetry points of the cubic phase, namely, X [$\mathbf{Q}_X = (H+1/2,K,L)$], M [$\mathbf{Q}_M = (H+1/2,K+1/2,L)$], and R [$\mathbf{Q}_R = (H+1/2,K+1/2,L+1/2)$] [16]. The location of these special points within the Brillouin zone of the high-temperature phase is shown in Fig. 1(a). The red arrow defines the high-symmetry cut $R \rightarrow \Gamma$, for which a

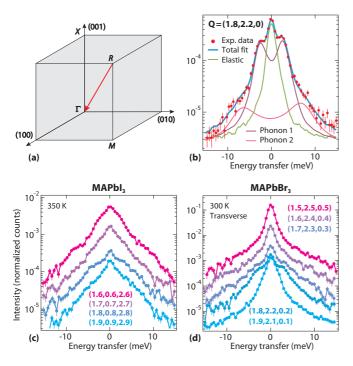*rcomin@mit.edu
†ted.sargent@utoronto.ca

FIG. 1. (a) Reciprocal space coordinates for the cubic structure, with high-symmetry points highlighted. The red arrow defines the trajectory followed for the measurements shown in panels (c) and (d). (b) Single IXS scan from MAPbBr$_3$ showing a representative overall fit profile and its decomposition into elastic line and phonon sidebands. (c),(d) A series of inelastic scans (scattered intensity vs energy transfer) of (c) MAPbI$_3$ and (d) MAPbBr$_3$ at selected wave vectors along the path defined in (a).

series of scans of the scattered intensity vs energy transfer is shown at selected wave vectors for MAPbI$_3$ [Fig. 1(c)] and MAPbBr$_3$ [Fig. 1(d)]. All the IXS scans presented in this study have been measured in the cubic phase, at $T = 350$ and 300 K for MAPbI$_3$ and MAPbBr$_3$, respectively.

The IXS profiles have been analyzed using a functional form which incorporates a sharp (δ function) elastic line together with a damped-harmonic-oscillator (DHO) functional form [17]:

$$I_{\text{DHO}}(\mathbf{Q},\omega) = I_{\text{el}}\delta(\omega) + I_{\text{inel}}\left[\frac{\Omega_{\mathbf{Q}}^2\Gamma_{\mathbf{Q}}}{\left(\omega^2 - \Omega_{\mathbf{Q}}^2\right)^2 + \omega^2\Gamma_{\mathbf{Q}}^2}\right], \quad (1)$$

where ω is the photon angular frequency, $\Omega_{\mathbf{Q}}$ and $\Gamma_{\mathbf{Q}}$ are the momentum-dependent phonon frequency and damping (inverse lifetime), and I_{el} and I_{inel} are the intensities of the elastic and inelastic terms, respectively. The final model function applied to the analysis of the experimental data is obtained after multiplication of Eq. (1) by the Bose factor $[n(\omega) + 1]$ to account for the temperature-dependent phonon population $[n(\omega)$ being the Bose-Einstein function] and subsequent convolution with the instrument resolution function (see also Supplemental Material [18]). An example of the fit profile based on this model function is shown in Fig. 1(b), where two sets of phonon sidebands can be resolved, together with the central elastic line. By applying this analysis to a complete data set of IXS experimental profiles, we have extracted the phonon dispersions in MAPbI$_3$ [Fig. 2(a)] and MAPbBr$_3$ for longitudinal [Fig. 2(b)] and transverse modes [Fig. 2(c)], along the $\Gamma \rightarrow X$ (red), $\Gamma \rightarrow M$ (green), and $\Gamma \rightarrow R$ (blue) directions. From numerical fits of the experimental data to Eq. (1), we have derived both the phonon frequency (markers) and broadening (vertical bars). The number of branches that we could resolve depends on the counting statistics and varies with the wave vector, but in all cases is limited by the range of energy transfer (± 15 meV). All the modes detected in our measurements correspond to low-energy excitations of the corner-sharing PbX$_3$ (X = I, Br) network, while the methylammonium internal vibrations generally appear at higher energies, although the translational and librational modes are found in the 10–20 meV energy range [19,20]. While it is possible that multiple modes are lumped together within individual fitted peaks, the broad energy
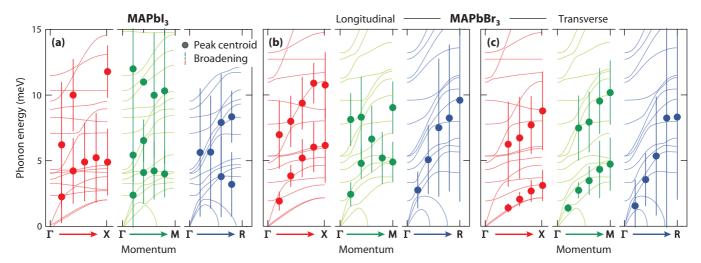

FIG. 2. (a) Experimental phonon dispersions (and calculated phonon bands overlaid) in MAPbI$_3$ along the three high-symmetry directions of the cubic phase, namely, $\Gamma \rightarrow X$ (red, left), $\Gamma \rightarrow M$ (green, center), and $\Gamma \rightarrow R$ (blue, right). Longitudinal and transverse modes are mixed due to the scattering geometry adopted for MAPbI$_3$. (b),(c) Experimental phonon dispersions (and calculated phonon bands overlaid) in MAPbBr$_3$ for (b) longitudinal and (c) transverse modes. Note: vertical bars reflect the experimental linewidth of phonon peaks and not the uncertainty on phonon frequency.

linewidths observed at various momenta might also indicate short phonon lifetimes, as recently observed using Raman spectroscopy [21]. The experimental phonon frequencies are compared to the theoretical vibrational band structure calculated using density functional theory in the frozen-phonon approximation (dispersions are overlaid in Fig. 2 and are in close agreement with those reported in Ref. [20]). The highest zone-center optical mode in MAPbI$_3$ is found at 7–7.5 meV, consistent with recent findings from a Raman/IR study [22]. Additionally, we note that the phonons become overdamped at the R point (this is particularly evident for MAPbBr$_3$), where numerical calculations predict an instability as signalled by the imaginary mode frequency, consistent with a displacive structural transition triggered by phonon condensation at the zone corner. A closer inspection of the longitudinal (LA) and transverse acoustic (TA) phonon dispersions in the vicinity of the Γ point (along the $\Gamma \rightarrow X$ direction) yields an estimate of the sound speed, which is a relevant quantity with a direct impact on the carrier mobility μ via electron-phonon coupling [23]. This analysis indicates a longitudinal (shear) sound speed of $v_l = 2714 \pm 650$ m/s ($v_s = 990 \pm 150$ m/s) in MAPbBr$_3$, while in MAPbI$_3$ this procedure is hindered by the inability to separate the LA and TA branches, which are mixed in due to the experimental geometry. From the calculated phonon bands we obtain $v_l \sim 3270$ and $v_s \sim 970$ m/s for MAPbI$_3$. The sound speed measured using IXS slightly underestimates the sound speed in the hydrodynamic regime (~ 1200 m/s) as measured using picosecond acoustic dynamics [24]. Further, these values suggest that the electron-phonon scattering rate τ^{-1} from acoustic modes, which is inversely
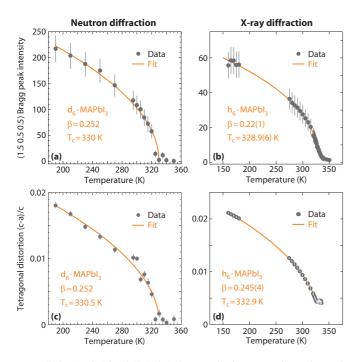
proportional to the sound speed ($\tau^{-1} \propto v^2$; see Ref. [25]), is slightly higher in MAPbI$_3$ than MAPbBr$_3$. However, it was recently pointed out that scattering of electrons from optical phonons is the dominant mechanism behind electron transport in these materials [21,25,26], likely explaining the long carrier lifetimes and diffusion lengths observed in high-quality crystals of hybrid halide perovskites [27].

In the second part of our study we examined the momentum fingerprints of the cubic-to-tetragonal structural transition and how the lowering of the lattice symmetry is unfolded in reciprocal space.

The nature of the cubic-tetragonal phase transition was also investigated using single crystal neutron diffraction at the Oak Ridge National Laboratory (ORNL) Spallation Neutron Source's TOPAZ instrument [28] for a deuterated MAPbI$_3$
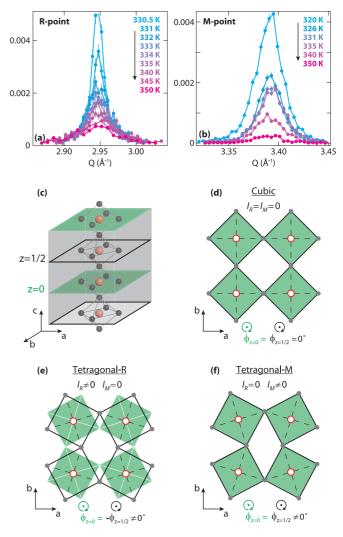

FIG. 4. Temperature-dependent momentum scans of MAPbI$_3$ at the (a) R and (b) M points above the cubic-to-tetragonal phase transition temperature. (c) Side view of the crystal structure, and (d)–(f) top view along the c axis highlighting the different octahedra rotation motifs for the (d) cubic (undistorted) phase, (e) tetragonal-R phase, and (f) tetragonal-M phase. Note that the two tetragonal phases have different unit cells (the one of the tetragonal-R structure is doubled along the c axis) and their order parameters are represented by the Bragg intensity at R and M points, respectively.

FIG. 3. (a) Cubic (3/2 1/2 1/2) superlattice Bragg intensity and (c) tetragonal distortion for single crystal d$_6$-MAPbI$_3$ measured by neutron diffraction on TOPAZ. (b) Cubic (3/2 1/2 1/2) superlattice Bragg intensity and (d) tetragonal distortion for polycrystalline h$_6$-MAPbI$_3$ measured by x-ray powder diffraction on the DuPont-Northwestern-Dow Collaborative Access Team (DND-CAT). Error bars in panels (c) and (d) are multiplied by a factor of 3 for clarity.

crystal (d_6-MAPbI$_3$) and synchrotron x-ray powder diffraction for a fully hydrogenated polycrystalline sample (h_6-MAPbI$_3$). The intensity of the (3/2 1/2 1/2) superlattice Bragg peak and the tetragonal distortion were measured to evaluate the critical behavior of the phase transition, and the results are shown in Fig. 3. Each set of data was fit to a power law, $I \sim (T_c - T)^{2\beta}$, where the factor of 2 in the exponent accounts for the fact that the superlattice intensity will scale as the square of the order parameter for the phase transition, where the order parameter is the rotation angle of the PbI$_6$ octahedra [29]. Similarly, the tetragonal strain is a secondary order parameter which is also expected to scale as the square of the order parameter for the phase transition [30]. The values of β vary from 0.22 to 0.252, where the mean-field result for a second-order phase transition is $\beta = 0.5$. The measured values are close to that expected for a tricritical phase transition, $\beta = 0.25$, which occurs at the intersection of lines of first-order and second-order phase transitions [31]. However, the presence of a distinct temperature range of cubic and tetragonal phase coexistence [32], and latent heat in heat capacity measurements [33], are only consistent with a first-order transition, suggesting that these materials are still on the first-order side of the tricritical point.

To complete our study, we have performed IXS scans in momentum space across the R and M points in MAPbI$_3$, as a function of temperature above the phase transition [Figs. 4(a) and 4(b)]. More specifically, we have scanned reciprocal space by sweeping the detector (and therefore the scattering) angle while in energy-resolved mode, i.e., collecting only the quasielastic scattering at $\omega = 0$ and at low momentum resolution (0.01 Å^{-1}) to maximize the sensitivity to weak scattering signals. Most importantly, the high energy resolution allows us to separate the quasielastic (quasistatic) component from the thermal diffuse scattering, which is inelastic in nature and cannot be avoided in energy-integrated measurements such as neutron or x-ray diffraction, as discussed above. At variance with previous reports [34], we find that the scattered intensity at the R point does not vanish above T_c, but persists up to 20 K away from the transition temperature, as shown in Fig. 4(a) (a similar behavior is found in MAPbBr$_3$; see Supplemental Material [18]). In MAPbI$_3$ we also detect weaker reflections at the M point [Fig. 4(b)], which suggests that, alongside the dominant lattice symmetry and its representative Bragg signatures, there are small regions with short-range-ordered puddles locally breaking cubic symmetry. Since our data at

$\omega = 0$ only reflect the static scattering (within the energy resolution of the IXS spectrometer), they demonstrate the existence of symmetry-breaking nanopuddles well above the thermodynamic structural transition temperature, in analogy with the phenomenology of the central peak in SrTiO$_3$ [35,36]. The associated temperature evolution of the forbidden superlattice reflection intensities (which in the cubic phase are ~2 orders of magnitude weaker than the allowed R-point Bragg reflection below T_c) and correlation lengths (see Supplemental Material [18]) suggests that these nanoislands initially nucleate around defects that break cubic symmetry and progressively grow in size, coalescing into long-range ordered structures near and below the phase transition. The formation of these cubic-symmetry-breaking domains therefore precedes the complete renormalization of the phonon frequency and the simultaneous condensation of the phonon mode into a static distortion. These two phenomena are *a priori* independent, and while the phonon softening mechanism is driven by a native instability of the cubic lattice, the short-ranged nanodomains likely reflect the nature of the symmetry-breaking defects, previously investigated [37,38]. This likely explains why we observe scattering intensity also at the M point, where no frozen-in phonon modes should be expected altogether.

In conclusion, the present study confirms the existence of a lattice instability at the R point, and elucidates the tricritical nature of the cubic-to-tetragonal phase transition. In addition, we uncover the presence of static and short-ranged noncubic nanoregions well above the structural transition and in the temperature range relevant for photovoltaic operation.

[1] G. Shirane and S. Hoshino, J. Phys. Soc. Jpn. **6**, 265 (1951).

[2] Y. Fujii, S. Hoshino, Y. Yamada, and G. Shirane, Phys. Rev. B **9**, 4549 (1974).

[3] S. R. Andrews, J. Phys. C **19**, 3721 (1986).

[4] U. J. Nicholls and R. A. Cowley, J. Phys. C **20**, 3417 (1987).

[5] S. D. Stranks and H. J. Snaith, Nat. Nanotechnol. **10**, 391 (2015).

[6] J. H. Noh, S. H. Im, J. H. Heo, T. N. Mandal, and S. I. Seok, Nano Lett. **13**, 1764 (2013).

[7] E. Mosconi, A. Amat, M. K. Nazeeruddin, M. Grtzel, and F. De Angelis, J. Phys. Chem. C **117**, 13902 (2013).

[8] R. Comin, G. Walters, E. S. Thibau, O. Voznyy, Z.-H. Lu, and E. H. Sargent, J. Mater. Chem. C **3**, 8839 (2015).

[9] H. Zhang, X. Qiao, Y. Shen, T. Moehl, S. M. Zakeeruddin, M. Grtzel, and M. Wang, J. Mater. Chem. A **3**, 11762 (2015).

[10] C. Quarti, E. Mosconi, and F. De Angelis, Chem. Mater. **26**, 6557 (2014).

[11] A. Poglitsch and D. Weber, J. Chem. Phys. **87**, 6373 (1987).

[12] T. S. Toellner, A. Alatas, and A. H. Said, J. Synch. Radiat. **18**, 605 (2011).

[13] A. H. Said, H. Sinn, and R. Divan, J. Synch. Radiat. **18**, 492 (2011).

[14] J. M. Kadro, K. Nonomura, D. Gachet, M. Grtzel, and A. Hagfeldt, Sci. Rep. **5**, 11654 (2015).

[15] M. I. Saidaminov, A. L. Abdelhady, B. Murali, E. Alarousu, V. M. Burlakov, W. Peng, I. Dursun, L. Wang, Y. He, G. Maculan, A. Goriely, T. Wu, O. F. Mohammed, and O. M. Bakr, Nat. Commun. **6**, 7586 (2015).

[16] Here, H, K, and L are integer indices, which are also used to label the reciprocal lattice location where measurements were performed.

[17] B. Fȧk and B. Dorner, Physica B **234-236**, 1107 (1997).

[18] See Supplemental Material at http://link.aps.org/supplemental/10.1103/PhysRevB.94.094301 for further details.

[19] C. Quarti, G. Grancini, E. Mosconi, P. Bruno, J. M. Ball, M. M. Lee, H. J. Snaith, A. Petrozza, and F. D. Angelis, J. Phys. Chem. Lett. **5**, 279 (2014).

[20] F. Brivio, J. M. Frost, J. M. Skelton, A. J. Jackson, O. J. Weber, M. T. Weller, A. R. Goñi, A. M. A. Leguy, P. R. F. Barnes, and A. Walsh, Phys. Rev. B **92**, 144308 (2015).

[21] A. M. A. Leguy, A. R. Goñi, J. M. Frost, J. Skelton, F. Brivio, X. Rodríguez-Martínez, O. J. Weber, A. Pallipurath, M. I. Alonso, M. Campoy-Quiles, M. T. Weller, J. Nelson, A. Walsh, and P. R. F. Barnes, Phys. Chem. Chem. Phys. (2016), doi:10.1039/C6CP03474H.

[22] M. A. Pérez-Osorio, R. L. Milot, M. R. Filip, J. B. Patel, L. M. Herz, M. B. Johnston, and F. Giustino, J. Phys. Chem. C **119**, 25703 (2015).

[23] S. Takagi, A. Toriumi, M. Iwase, and H. Tango, IEEE Trans. Electron Devices **41**, 2363 (1994).

[24] Z. Guo, S. J. Yoon, J. S. Manser, P. V. Kamat, and T. Luo, J Phys. Chem. C **120**, 6394 (2016).

[25] A. Filippetti, A. Mattoni, C. Caddeo, M. I. Saba, and P. Delugas, Phys. Chem. Chem. Phys. **18**, 15352 (2016).

[26] A. D. Wright, C. Verdi, R. L. Milot, G. E. Eperon, M. A. Pérez-Osorio, H. J. Snaith, F. Giustino, M. B. Johnston, and L. M. Herz, Nat. Commun. **7**, 11755 (2016).

[27] D. Shi, V. Adinolfi, R. Comin, M. Yuan, E. Alarousu, A. Buin, Y. Chen, S. Hoogland, A. Rothenberger, K. Katsiev, Y. Losovyj, X. Zhang, P. A. Dowben, O. F. Mohammed, E. H. Sargent, and O. M. Bakr, Science **347**, 519 (2015).

[28] A. J. Schultz, M. R. V. Jørgensen, X. Wang, R. L. Mikkelson, D. J. Mikkelson, V. E. Lynch, P. F. Peterson, M. L. Green, and C. M. Hoffmann, J. Appl. Crystallogr. **47**, 915 (2014).

[29] Y. Kawamura, H. Mashiyama, and K. Hasebe, J. Phys. Soc. Jpn. **71**, 1694 (2002).

[30] J. C. Slonczewski and H. Thomas, Phys. Rev. B **1**, 3599 (1970).

[31] J.-C. Toledano and P. Toledano, *The Landau Theory of Phase Transitions* (World Scientific, Teaneck, NJ, 1987).

[32] P. Whitfield, N. Herron, W. Guise, K. Page, Y. Q. Cheng, I. Milas, and M. Crawford (unpublished).

[33] N. Onoda-Yamamuro, T. Matsuo, and H. Suga, J. Phys. Chem. Solids **51**, 1383 (1990).

[34] M. T. Weller, O. J. Weber, P. F. Henry, A. M. D. Pumpo, and T. C. Hansen, Chem. Commun. **51**, 4180 (2015).

[35] M. Holt, M. Sutton, P. Zschack, H. Hong, and T.-C. Chiang, Phys. Rev. Lett. **98**, 065501 (2007).

[36] H. Hong, R. Xu, A. Alatas, M. Holt, and T.-C. Chiang, Phys. Rev. B **78**, 104121 (2008).

[37] A. Buin, P. Pietsch, J. Xu, O. Voznyy, A. H. Ip, R. Comin, and E. H. Sargent, Nano Lett. **14**, 6281 (2014).

[38] A. Buin, R. Comin, J. Xu, A. H. Ip, and E. H. Sargent, Chem. Mater. **27**, 4405 (2015).